Chapter-5

Structural and magnetic properties of $Cu_{1-x}Zn_xFe_2O_4$ nano-powders synthesized by oxalate based precursor method

5.1 Introduction

Ferrites are an important class of technological materials that have been recognized to have significant potential applications ranging from millimeter wave integrated circuitry to transformer cores and magnetic recording [1]. The technological importance of ferrites increased continuously as many discoveries required the use of magnetic materials [2]. Ferrite thin films have the potential to replace bulky external magnets in current devices. The study of ferrite thin films is of interest due to the fundamental differences in their magnetic and electronic properties from the bulk counterparts [3]. Copper zinc ferrites crystallize in cubic spinel structure. The distribution of cations can be influenced by several factors such as the chemical composition, ionic radius, electronic configuration, and electrostatic energy, method of preparation and preparation conditions [4].

Nanocrystalline Cu-Zn ferrite have been extensively investigated due to their potential applications in non-resonant device, radio frequency circuits, rod antennas, high quality filters, transformer cores, read/write heads for high speed digital tapes and operating devices [5, 6]. Copper ferrite ($CuFe_2O_4$) is an interesting material and has been widely used for various applications, such as catalysts for environment [7], gas sensor [8], and hydrogen production [9]. Magnetic and electrical properties of Cu ferrites vary greatly with the change chemical component and cation distribution. For instance, most of bulk $CuFe_2O_4$ has an inverse spinel structure, with 85% Cu^{2+} occupying B sites [10], whereas $ZnFe_2O_4$ is usually assumed to be a completely normal spinel and Zn^{2+} ions preferentially occupy A sites while Fe^{3+} ions would be displaced from A sites for B sites. [11]. Zn-substitution results to a change of cations in chemical composition and a different distribution of cations between A and B sites.

Consequently the magnetic and electrical properties of spinel ferrites will change with changing cation distribution. However, there are no reports on the synthesis and characterize of Cu-Zn ferrites nanoparticles using oxalic acid precursor method in the literatures. Therefore, in this work we tried to synthesize Cu-Zn ferrite to study the structural and magnetic properties.

5.2 Experimental procedures

5.2.1 Synthesis of $Cu_{1-x}Zn_xFe_2O_4$ (x = 0.0, 0.2, 0.4, 0.6, 0.8) nanopowders.

Nanocrystalline powders of $Cu_{1-x}Zn_xFe_2O_4$ (x = 0.0, 0.2, 0.4, 0.6, 0.8) were prepared by oxalic acid based precursor method [12, 13]. All of the chemicals were analytical grade from Sigma–Aldrich with purity ≥ 99% and were used without any further purification. In a typical procedure, the copper hydrate $Cu(NO_3)_2 \cdot 6H_2O$, zinc nitrate hydrate $Zn(NO_3)_2 \cdot 6H_2O$, ferric nitrate nonahydrate $Fe(NO_3)_3 \cdot 9H_2O$wereused as starting materials. Stoichiometric amounts of metal nitrates were dissolved in deionized water to get clear solution. The obtained aqueous solution of metal nitrates was mixed with oxalic acid in a molar ratio ranging from 1:3 to 1:0.15. The mixture solution were moved on to magnetic stirrer and stirred for 2 h at room temperature. The reaction mixtures turned turbid by varying molar ratios 1:3 and 1:2. When the molar ratio was further lowered to 1:1, precursor solution showed different colour shades. The resultant mixtures were evaporated on a hot plate at 150 ˚C for 2 h. The obtained raw powders were thermally heat treated at 300 ◦C for 4 h to get the single phase nanocrystalline Cu-Zn ferrites.

5.2.2 Characterization of $Cu_{1-x}Zn_xFe_2O_4$ (x = 0.0, 0.2, 0.4, 0.6, 0.8) nanopowders

The structural characterization of the prepared Cu-Zn ferrite nanopowders was carried out using Philips X-ray diffraction system with Ni filter using Cu –Kα radiation (wave length λ= 1.54 A^o). The average particle size *D* was calculated using most intense peak (311) employing the Scherer formula. The particle size and morphology was carried out using FE-SEM (model JSM-7000F) manufactured by JEOL Ltd. The FE-SEM was linked to an EDS/INCA 350 (energy dispersive X-ray analyzer) manufactured by Oxford Instruments Ltd. The structural changes with calcination temperature are observed by ABB Bomem MB 102 infrared spectrometer equipped with CsI optics and DTGS detector. The samples were mixed with KBr and made in the form of pellets and recorded at 4 cm^{-1} resolution (10 consecutive scans were averaged for each spectrum), giving the spectra in the 4000 - 200 cm^{-1} range. Magnetic measurements were performed using Lakeshore VSM 7410. Magnetic hysteresis loops were measured at room temperature with maximal applied magnetic fields of 10 kOe. Maximum magnetization, coercivity and remanent magnetization were observed from the hysteresis loops.

5.3 Results and discussions

5.3.1 Structural characterization

Fig. 5. 1 shows the X-ray diffractograms of $Cu_{1-x}Zn_xFe_2O_4$ (x = 0.0, 0.2, 0.4, 0.6, 0.8). The XRD patterns clearly indicate that the prepared samples contain cubic spinel structure only. From the XRD it can be clearly seen that no secondary phases exists and the prepared ferrite nanopowders contains only single phase spinel structure. All the peaks of the XRD pattern are indexed as reported in JCPDS cards.

A close examination of XRD patterns as shown in Fig.5.2 reveals that the diffraction peaks became broader with increasing Zn content *x*, which may be attributed due to the reduced nanocrystallite size with Zn doping. It can be clearly observed from Fig. 5.2 that the full-width at half maximum (FWHM) increases upon increasing Zn doping and it results in the decrease of particle size. The probable reason for this kind effect may be due to the reaction time and temperature during the synthesis process. Generally in the case of nano ferrites, behavior such as decrease in the particle with the increase in the doping concentration is seen quite common [14, 15]. The sizes of crystallite size of all the samples is evaluated by measuring the FWHM of the most intense peak (311) using the Scherer formula (equation 5.1).

$$D = \frac{0.9\lambda}{\beta \cos\theta} \tag{5.1}$$

where, D is the average crystalline size, λ is the X-ray wavelength, β is the angular line width of half maximum intensity and θ is the Bragg angle in degrees.

The observed particle size of $Cu_{1-x}Zn_xFe_2O_4$ (x = 0.0, 0.2, 0.4, 0.6, 0.8) are listed in Table 5.1. Furthermore, it is observed from Table 5.1 that, the particle size D decreases with increasing Zn content x and is plotted as shown in the Figure 5.3.

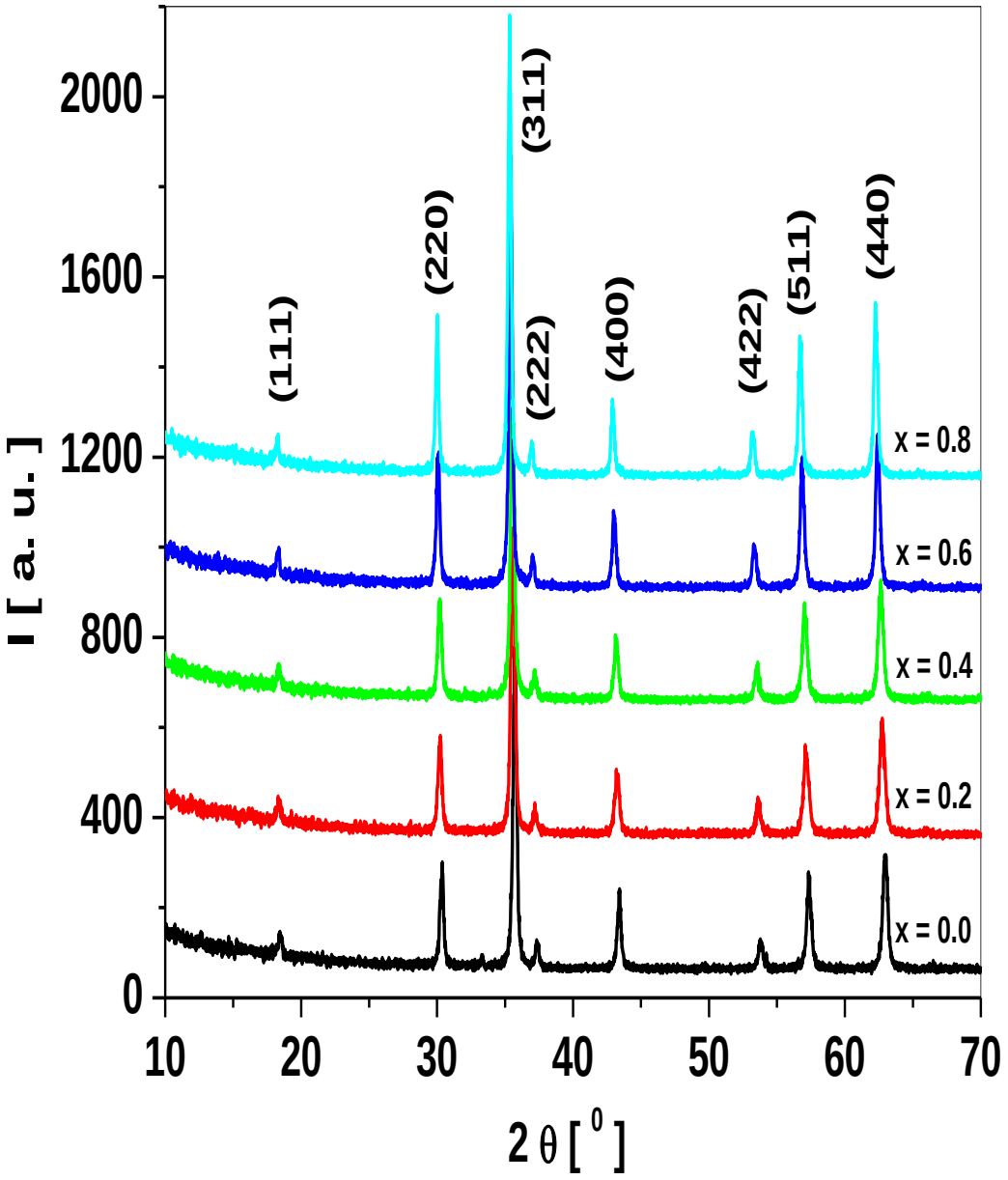

Figure 5.1: X-ray diffraction pattern of $Cu_{1-x}Zn_xFe_2O_4$ (x = 0.0, 0.2, 0.4, 0.6, and 0.8) nanoparticles.

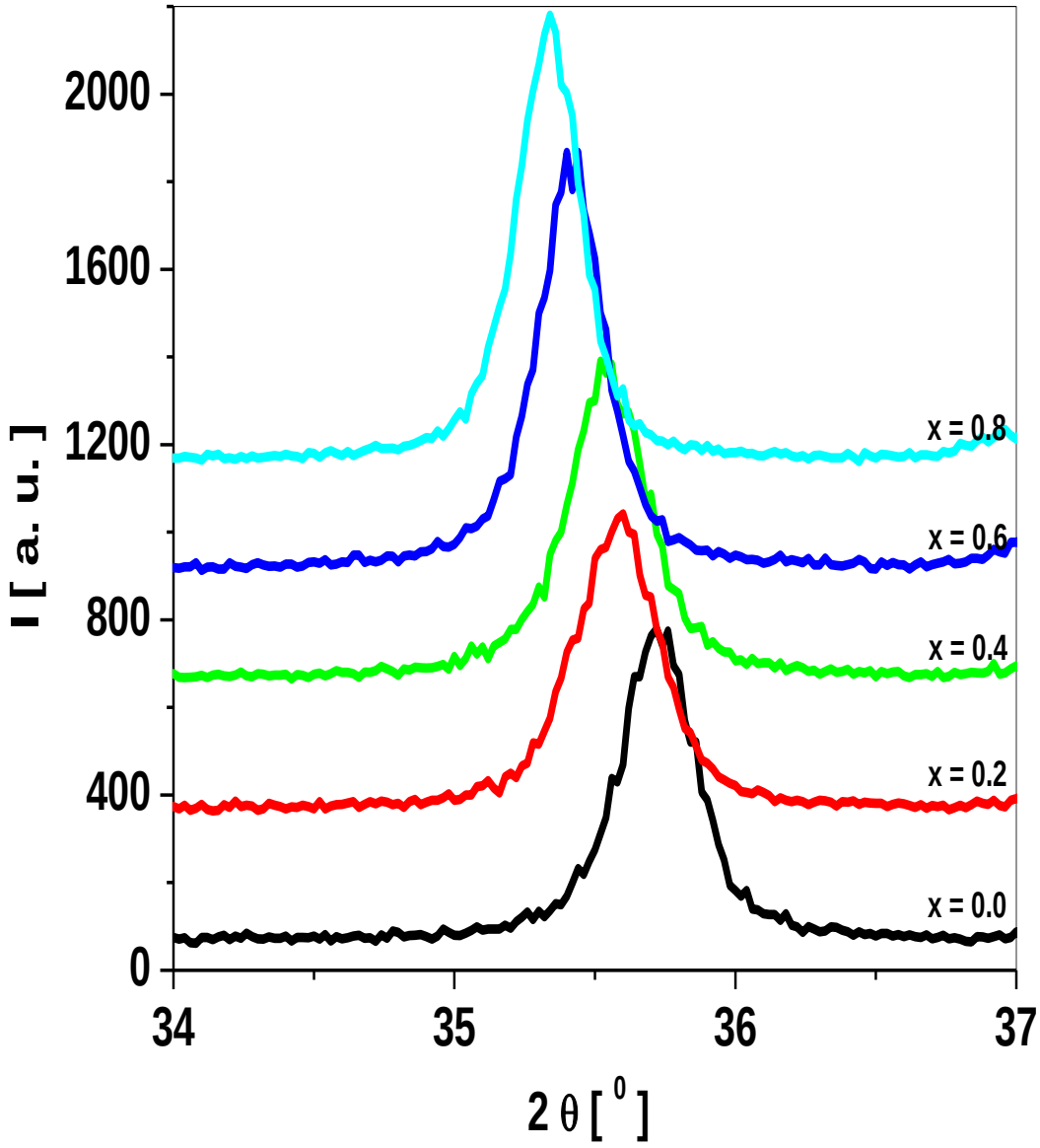

Figure 5.2: X-ray diffraction pattern of high intensity (311) peak $Cu_{1-x}Zn_xFe_2O_4$ (*x* = 0.0, 0.2, 0.4, 0.6, 0.8) nanoparticles.

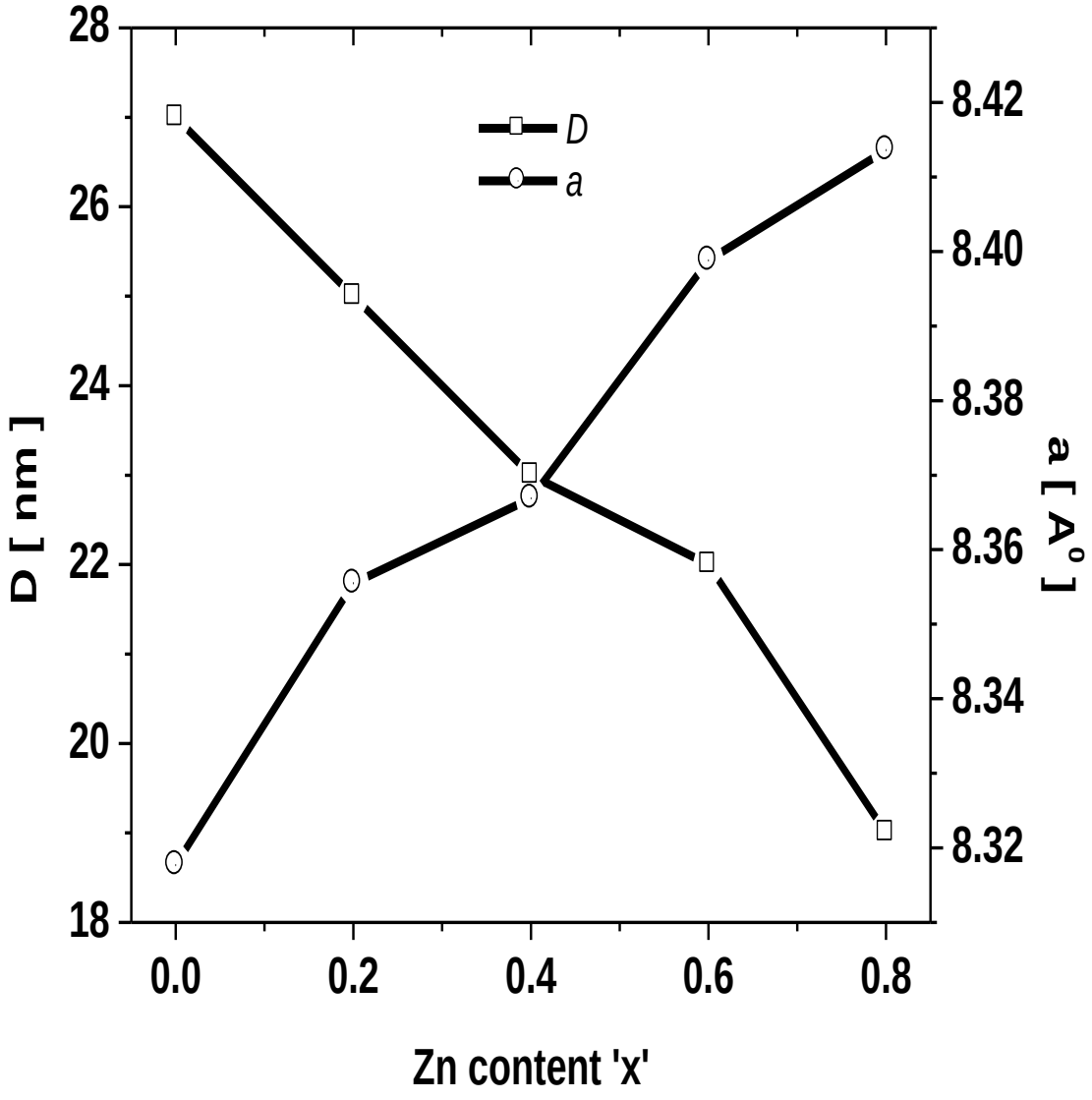

Figure 5.3: Particle size and lattice values of $Cu_{1-x}Zn_xFe_2O_4$ (x = 0.0, 0.2, 0.4, 0.6, and 0.8) nanoparticles.

The values for lattice constants were obtained for all the $Cu_{1-x}Zn_xFe_2O_4$ nanoparticles using the most intense (311) peak from XRD data using the equation 2. The values of lattice constants are listed in Table 5.1 and plotted is as shown in Figure 5.3.

$$a = d\sqrt{N} \qquad (5.2)$$

where *a* is lattice constant, *d* is inter planar spacing (distance between adjacent *hkl planes* - miller indices) and $N = h^2 + k^2 + l^2$.

The lattice constant *a* is observed to increase with increasing the non-magnetic Zn content *x*. This behavior of lattice constant with Zn content *x* is explained on the basis of difference in the ionic radii of Cu^{2+} and Zn^{2+}. The $Cu_{1-x}Zn_xFe_2O_4$ system has a cubic spinel configuration with unit cell consisting of eight formula units of the form $(Zn_xFe_{1-x})^A$ $[Cu_{1-x}Fe_{1+x}]^B$ O_4. The Cu^{2+} ions have a preference for the octahedral sites and Zn^{2+} ions have preference for the tetrahedral sites. The observed linear increasing of lattice constant with Zn content *x* can be attributed to the large ionic radius of Zn^{2+} (0.84 A^0) as compared to the ionic radius of Cu^{2+} (0.79 A^0). The larger ionic radii Zn^{2+} atoms replaces the smaller ionic radii Cu^{2+} atoms and thus the lattice parameters shows increasing trend with increasing non-magnetic Zn content in $CuFe_2O_4$. A similar linear variation of lattice constant has been observedby Patange et. al., [16].

The X-ray density of the $Cu_{1-x}Zn_xFe_2O_4$ nanoferrite samples has been calculated from the molecular weight and the volumes of the unit cell using the equation 5.3.

$$d_x = \frac{8M}{Na^3}[g/cm^3] \qquad (5.3)$$

where 8 represents the number of molecules in a unit cell of spinel lattice, *M* is molecular weight, *N* is Avogadro's number and *a* is lattice parameter.

The values of X-ray density '*dx*' are given in Table 5.1. It can be seen from Table 5.1 that X-ray density increases with increasing zinc content *x*. The increase in X-ray density can be related with the lattice constant. In the present series of Cu–Zn spinel ferrites, the lattice constant increases with Zn^{2+} composition *x*. Due to increase in lattice constant, X-ray density should have been decreased, but in the present case molecular weight increases which overtake the increase in volume of the unit cell and hence X-ray density increases with Zn content *x*.

Table.5.1: Particle size *D*, Lattice values *a*, X-ray density d_x of $Cu_{1-x}Zn_xFe_2O_4$ (x = 0.0, 0.2, 0.4, 0.6, 0.8) nanoparticles.

X	D [nm]	a [A^0]	d_x [g / cm^3]
0.0	27	8.318	5.525
0.2	25	8.356	5.548
0.4	26	8.367	5.444
0.6	22	8.399	5.391
0.8	19	8.414	5.371

The distance between magnetic ions at tetrahedral A (L_A) and octahedral B (L_B) sites was calculated using equations 5.4 and 5.5. The variation of hopping length L_A and L_B is also shown in Figure 5.4. Both L_A and L_B increases with Zn content x. This may be attributed to the increase in lattice constant of the samples and also suggests that the jumping probability of ions is increasing.

The bond length of tetrahedral (A) site d_{Ax} (shortest distance between A-site cation and oxygen ion) and octahedral [B] site d_{Bx} (shortest distance between B-site cation and oxygen ion), tetrahedral edge d_{AXE}, shared octahedral edge d_{BXE} and unshared octahedral edge d_{BXEU} can be calculated by putting the experimental values of lattice parameter 'a' and oxygen positional parameter 'u' of each sample using equations 5.6 to 5.10. The values calculated from above mentioned equation are presented in Table 5.2. It indicate that the tetrahedral bond length d_{AX} and octahedral bond length d_{BX} increases as Zn^{2+} content 'x' increases as shown in Figure 5.5. The tetrahedral edge d_{AXE}, shared octahedral edge d_{BXE}, unshared octahedral edge d_{BXEU} does not vary much with increasing Zn composition. This could be related to the radius of Ni^{2+}, Zn^{2+} and Fe^{3+} ions.

$$L_A = \left(\frac{\sqrt{3}}{4}\right)a \tag{5.4}$$

$$L_B = \left(\frac{\sqrt{2}}{4}\right)a \tag{5.5}$$

$$d_{Ax} = \left(u - \frac{1}{4}\right)a\sqrt{3} \tag{5.6}$$

$$(d_{BX}) = aX\sqrt{\left(3u^2 - \frac{11}{4}u + \frac{43}{64}\right)} \tag{5.7}$$

$$d_{AE} = (2u - \frac{1}{2})a\sqrt{2} \tag{5.8}$$

$$(d_{BE})_{shared} = (1 - 2u)a\sqrt{2} \tag{5.9}$$

$$(d_{BE})_{unshared} = aX\sqrt{\left(4u^2 - 3u + \frac{11}{16}\right)} \tag{5.10}$$

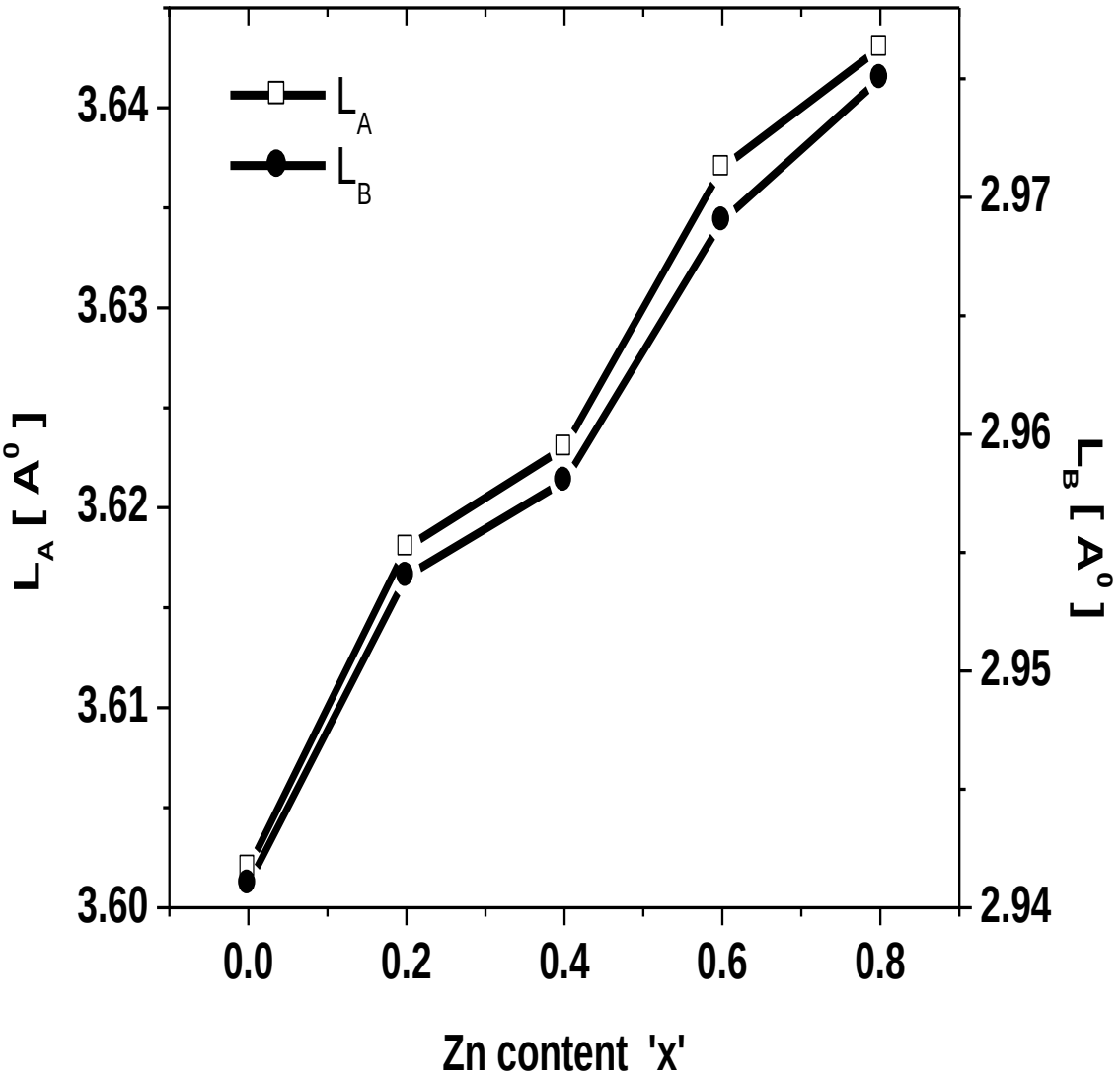

Figure 5.4: Variation of hopping length (L_A and L_B) $Cu_{1-x}Zn_xFe_2O_4$ (x = 0.0, 0.2, 0.4, 0.6, 0.8) nanoparticles.

Table 5.2: Tetrahedral bond (d_{AX}), octahedral bond (d_{BX}), tetra edge (d_{AXE}) and octa edge (d_{BXE}) (shared and unshared) of $Cu_{1-x}Zn_xFe_2O_4$ (x = 0.0, 0.2, 0.4, 0.6, 0.8) nanoparticles.

X	d_{AX} (Å)	d_{BX} (Å)	Edges		
			Tetra edge (Å)	Octa edge d_{BXE} (Å)	
			d_{AXE}	Shared	Unshared
0.0	1.887	2.033	3.081	2.799	2.948
0.2	1.896	2.042	3.095	2.812	2.962
0.4	1.898	2.045	3.100	2.816	2.966
0.6	1.906	2.053	3.111	2.826	2.977
0.8	1.909	2.056	3.170	2.831	2.982

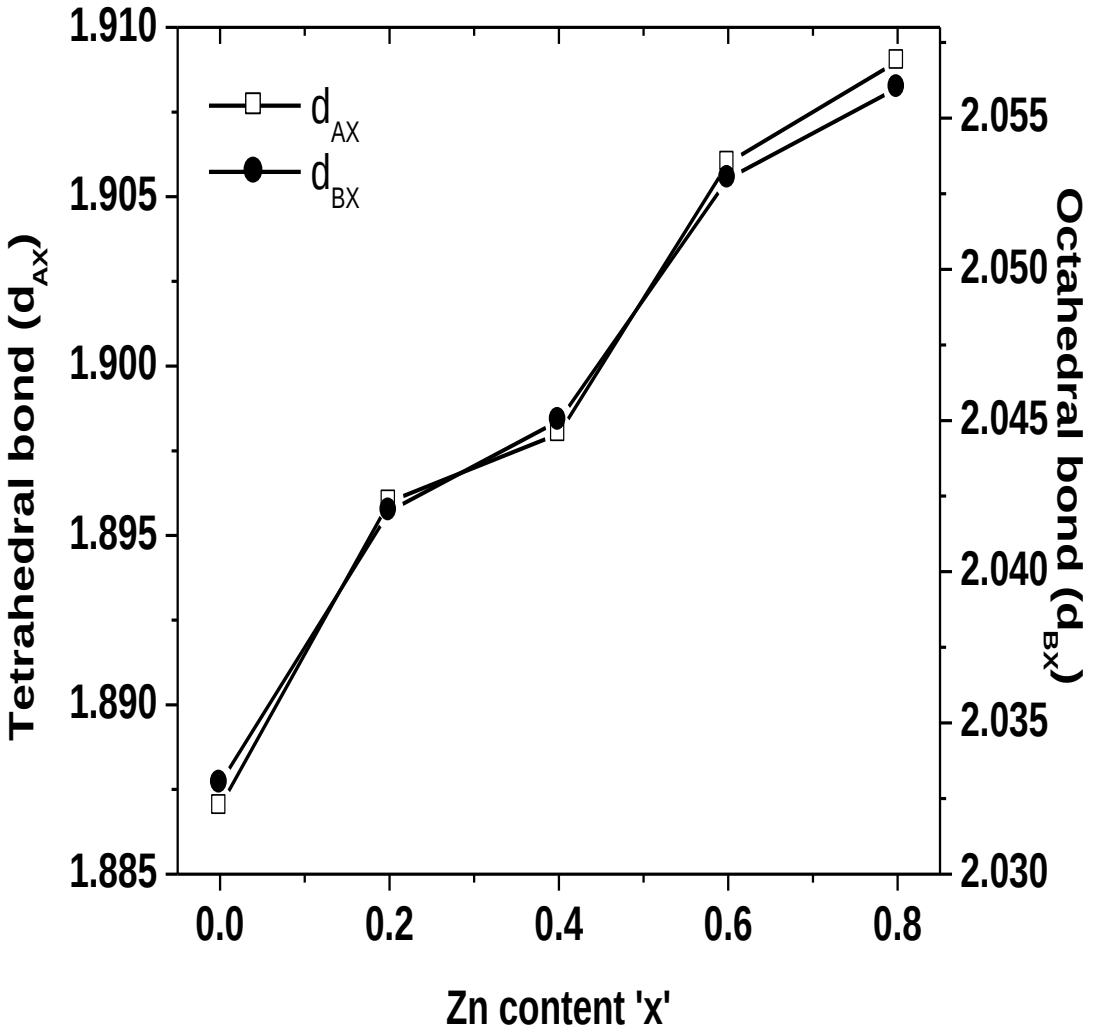

Figure 5.5: Effect of Tetrahedral bond (d_{AX}), octahedral bond (d_{BX}) on $Cu_{1-x}Zn_xFe_2O_4$ (x = 0.0, 0.2, 0.4, 0.6, 0.8) nanoparticles.

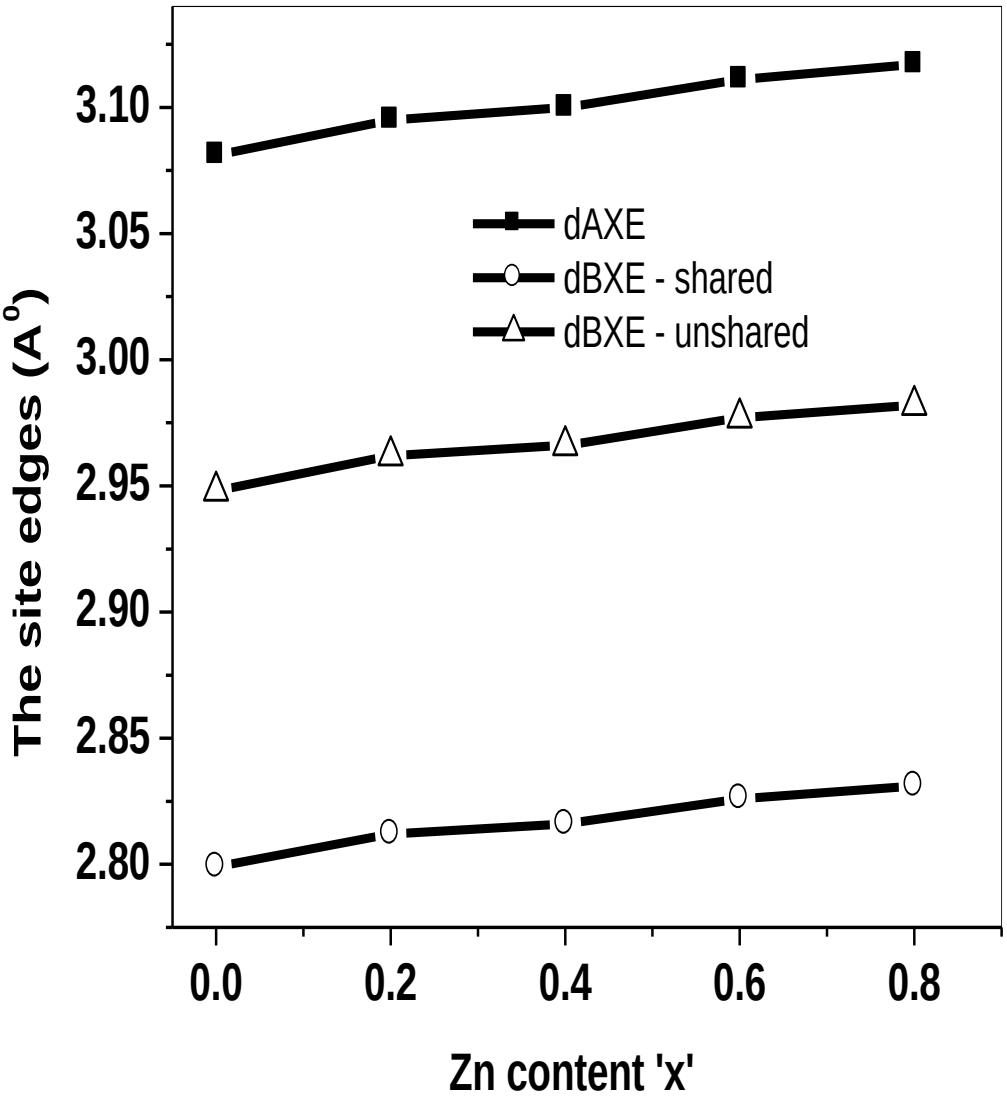

Figure 5.6: Effect of tetra edge (d_{AXE}) and octa edge (d_{BXE}) (shared and unshared) on $Cu_{1-x}Zn_xFe_2O_4$ (x = 0.0, 0.2, 0.4, 0.6, 0.8) nanoparticles.

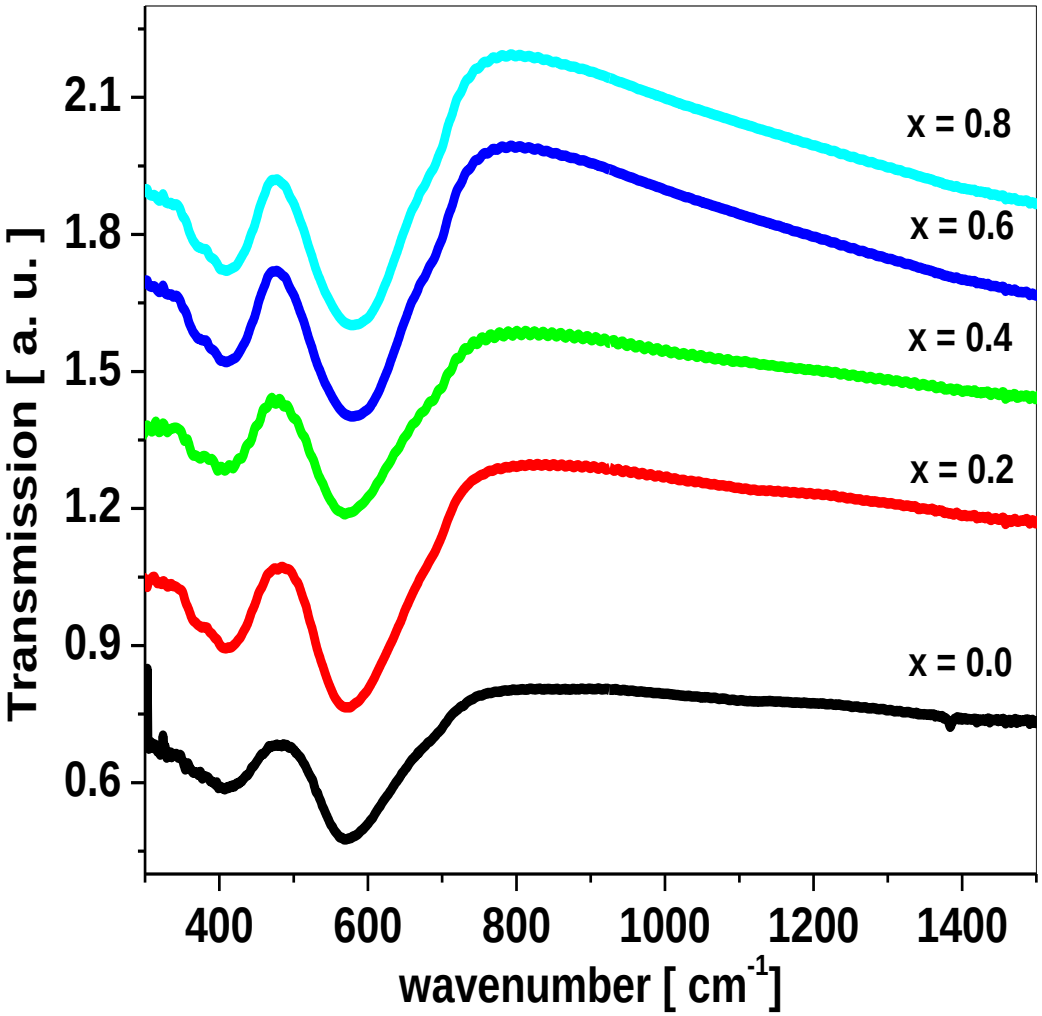

Figure 5.7: IR spectra of $Cu_{1-x}Zn_xFe_2O_4$ (x = 0.0, 0.2, 0.4, 0.6, and 0.8) nanoparticles.

Figure 5.7 gives the IR absorption spectra of the investigated ferrite, from which it can be seen that there are only two bands corresponding to the characteristic feature of ferrites. The values of the absorption band frequency are given in Table 5.3. The difference in positions of the bands for the various compositions was expected because of the difference in the distances for the octahedral and tetrahedral ions [17]. According to Waldron, the vibrations of the unit cell of cubic spinel can be constructed in the tetrahedral (A) sites and the octahedral [B] site. The spectra indicate the presence of two absorption bands, ν_1 and ν_2 in the range from 350 to 600 cm^{-1}, which is the common feature in all spinel structure. The ν_1 is attributed to the stretching vibration of Fe^{3+}–O_2^- in the tetrahedral complexes and the ν_2 to that of octahedral complexes.

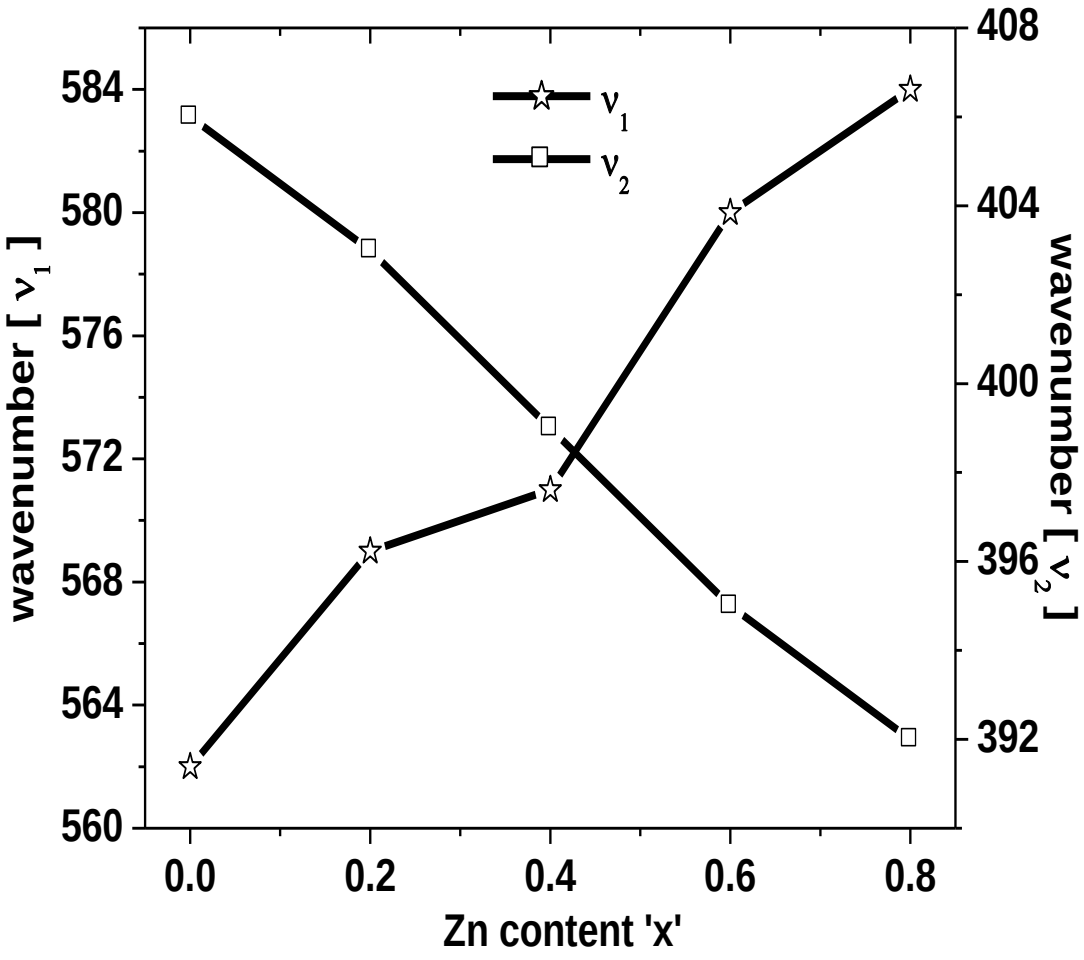

Figure 5.8: Variation of IR peak position v_1 and v_2 (cm^{-1}) for $Cu_{1-x}Zn_xFe_2O_4$ (x = 0.0, 0.2, 0.4, 0.6, 0.8) nanoparticles.

The position and intensities of ν_1 and ν_2, due to the difference in the Fe^{3+}–O_2^- distances for the tetrahedral and octahedral sites, change slightly with *x*. It is seen that the absorption band ν_1 linearly increases with the increase in content of Zn ions while band ν_2 decreases. As Zn^{2+} ions entirely occupy the tetrahedral sites and the Fe^{3+} ions in the octahedral sites increases. Therefore, the radius of tetrahedron becomes larger and that of octahedral hardly change with the content of the Zn ions. This may be one of the reasons for explaining the variance of bands ν_1 and ν_2. The bands ν_1 shift towards the higher frequency side and the bands ν_2 slightly shift towards lower frequency side with increase in Zn content due to the increase in site radius that decreases the fundamental frequency and hence the central frequency should shift towards the lower frequency side and viseversa for ν_2. Our results on infrared are similar to that of ceramically prepared samples of Mn–Ni–Zn by Bhise et al. [18].

Table 5.3: Variation of band position of ν_1 and ν_2 (cm^{-1}) for $Cu_{1-x}Zn_xFe_2O_4$ (x = 0.0, 0.2, 0.4, 0.6, 0.8) nanoparticles.

x	ν_1[cm^{-1}]	ν_2[cm^{-1}]
0.0	562	406
0.2	569	403
0.4	571	399
0.6	580	395
0.8	584	392

The shift in the band positions v_1 and v_2 suggests the structural changes are taken place with increasing Zn doping concentration.

Figure 5.9 shows SEM images of typical $Cu_{1-x}Zn_xFe_2O_4$ (x = 0.0 and 0.8) nanoparticles. As can be seen in Figure 5.9 (a) and (b), the microstructure of Cu Zn ferrite is homogeneous. The microstructures of the substituted Ni Zn ferrites depicted in Figure 4.9 (a) reveal a virtually uniform grain size and a homogeneous morphology. According to these micrographs, the microstructure is mainly influenced by the Zn substitution in Cu ferrite. It is observed that porosity affects the magnetic properties of the prepared nano ferrites. The particles are equally distributed and the measurement of particle size is clear. Therefore the observed particle size from the XRD measurements is very well in agreement with SEM analysis.

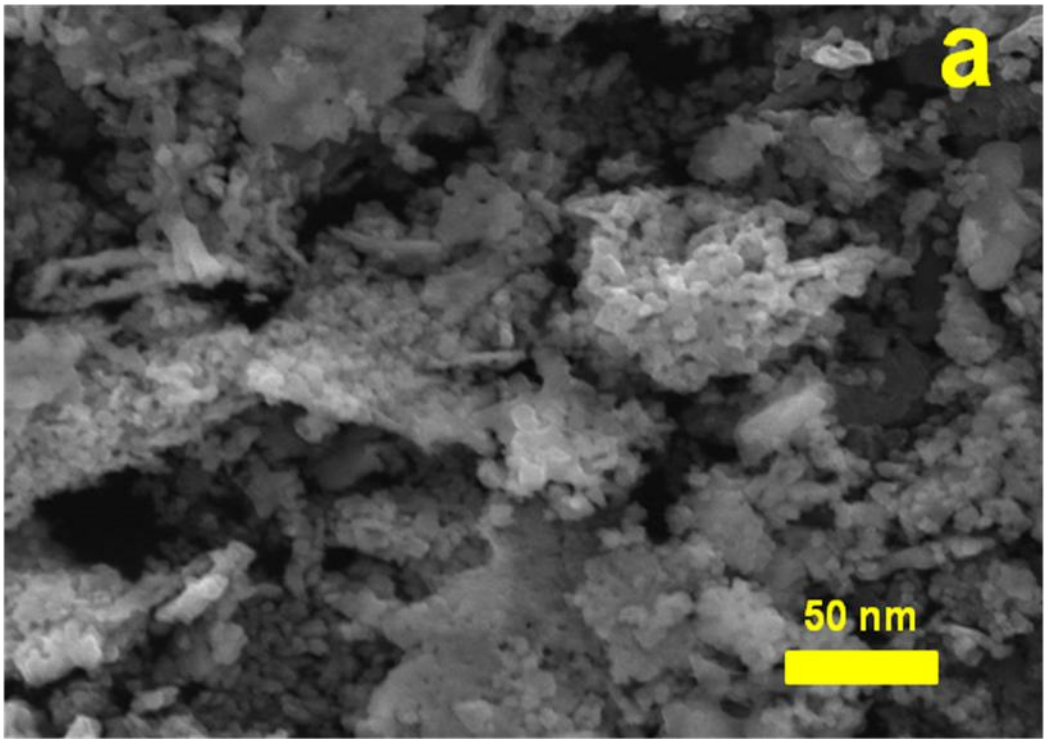

Figure 5.9(a): SEM image of $Cu_{1-x}Zn_xFe_2O_4$ (a) x = 0.0 nanoparticle.

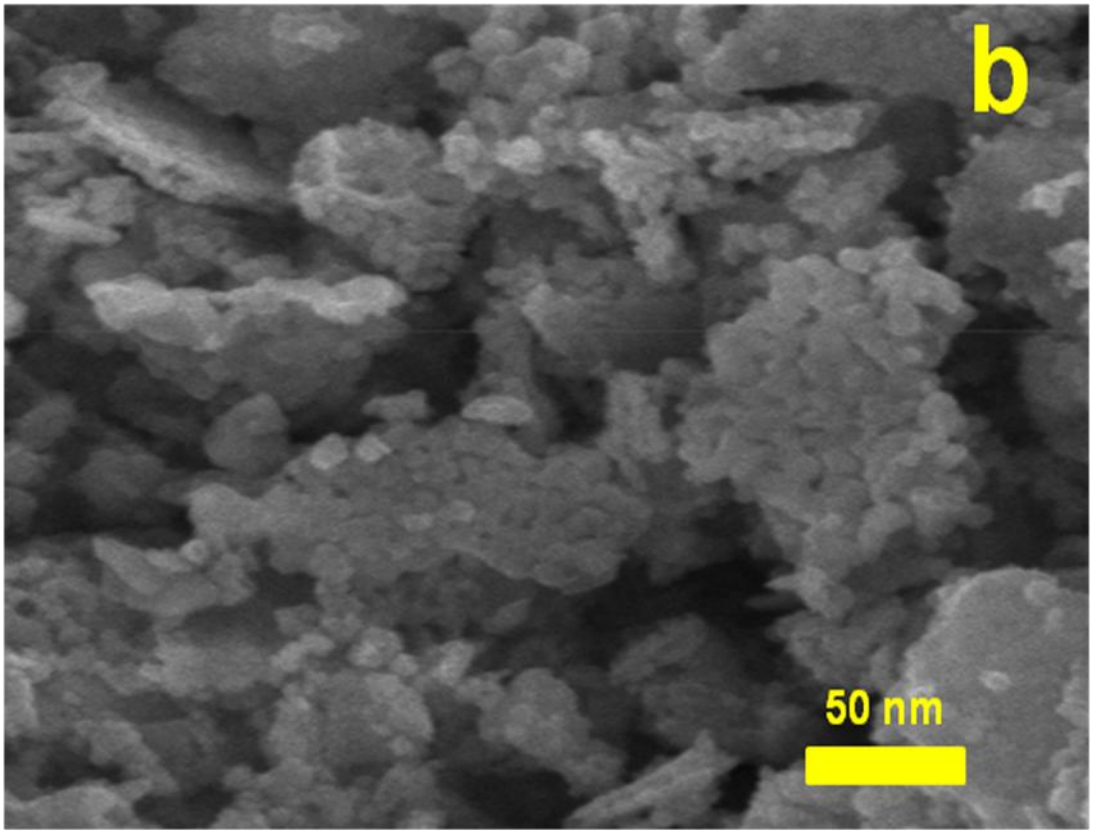

Figure 5.9(b): SEM image of $Cu_{1-x}Zn_xFe_2O_4$ (b) x = 0.8 nanoparticle.

5.3.2 Magnetic properties

Hysteresis loops for zinc substituting $CuFe_2O_4$ nanoferrites at room temperature are shown in Figure 5.10. The values of saturation magnetization (M_s), coercivity (H_c) and remanence (M_r) are given in Table 5.4. The magnetic properties of Cu-Zn nanoferrites vary with changing zinc content. The variation of magnetic properties of $Cu_{1-x}Zn_xFe_2O_4$ nanoferrites can be understood in term of cation distribution and exchange interactions between spinel lattices.

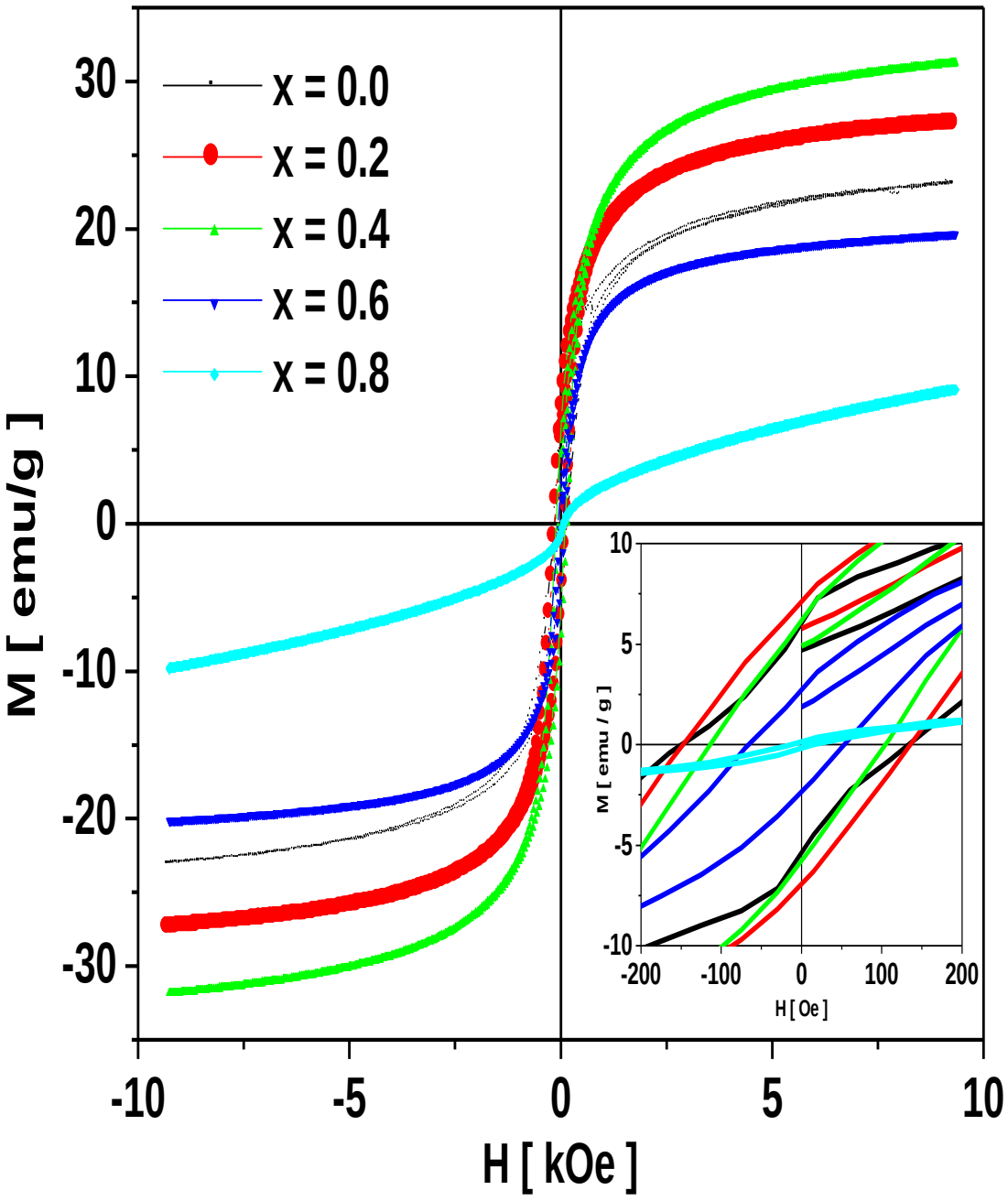

Figure 5.10: Hysteresis curves for the samples $Cu_{1-x}Zn_xFe_2O_4$ (x = 0.0, 0.2, 0.4, 0.6, and 0.8) nanoparticles

The $Cu_{1-x}Zn_xFe_2O_4$ nanoferrites with $x \leq 0.6$ exhibit ferromagnetic behavior, whereas for $x = 0.8$ nanoferrites display paramagnetic character with zero coercivity, zero remanence and non-saturated magnetization. The saturation magnetization initially increases with increasing zinc content and reaches a maximum (31.5 emu/g) and then decreases. The increase in saturation magnetization may be attributed to the fact that, small amount of Zn ions substituted for Cu occupy A sites displaces Fe ions from A sites to B sites, which increases the content of Fe ions in B sites. This leads to an increase of magnetic moment in B-site and a decrease of magnetic moment in A-site. So the net magnetization increases, which is consistent with the increase of saturation magnetization. With further increase nonmagnetic Zn ions substitution, the dilution at the A sites increases. This results in the breakdown of the ferromagnetic phase at $x \leq 0.4$. For $Cu_{1-x}Zn_xFe_2O_4$ ($x = 0.6$ and 0.8), the triangular spin arrangement on B-sites is suitable and this causes a reduction in A-B interaction and an increase of B-B interaction. Therefore, the decrease of saturation magnetization can be explained on the basis of three sublattice Yafet-Kittel model [19].

As shown in Table 5.4, coercivity (H_c) continuously reduced with increasing Zn ions content. These magnetic behaviors of ferrite depend intirely on the spinel structure. For instance, normal spinel ferrite shows an antiferromagnetically ordering, while inverse spinel ferrite shows a ferromagnetic ordering. With increasing Zn ions concentration, a transformation from inverse spinel structure of $CuFe_2O_4$ ferrite to normal spinel structure of $ZnFe_2O_4$ ferrite will arises gradually.

Variation of saturation magnetization with Zn content is as shown in Figure 5.11. The observed variations can be explained on the basis of cations distribution and exchange interaction between Fe ions and between Zn ions at the tetrahedral A and octahedral B sites. When Zn ions are introduced at the expense of Cu ions, some of the Fe ions migrate from A – to the B- sites. This increases the Fe ion concentration at B-sites. As a result, the magnetic moment of B sub-lattices increases with increasing Zn concentration up to $x \leq 0.4$. However, as Zn concentration increases, the Fe ions left at A-site being small in number, the A–B interaction experienced by B-site iron ions decreases. Also, the increased number of Fe ions at the B-site increases the B–B interaction, resulting in spin canting [20]. The decrease in the B sub-lattice moment, interpreted as a spin departure from co-linearity, causes the effect known as canting. Magnetization values for the present Cu-Zn nanoferrites were observed to be smaller than that of ceramically prepared samples [21]. This might be due to several reasons such as Nanocrystalline nature, surface disorder, modified cationic distribution etc. [22].

Table.5.4: Coercivity H_c, remanence magnetization M_r, maximum magnetization at M, for $Cu_{1-x}Zn_xFe_2O_4$ (x = 0.0, 0.2, 0.4, 0.6, 0.8) nanoparticles observed from hysteresis loops.

x	H_c [Oe]	M_r [emu/g]	M_s [emu/g]
0.0	146	5.7	23.2
0.2	141	7.1	27.5
0.4	108	5.9	31.5
0.6	61	2.5	20.1
0.8	15	0.2	9.6

Figure 5.12 shows the change in the coercive force (H_c) with Zn ion concentration. The coercivity is influenced by factors such as magnetocrystalline anisotropy, micro-strain, magnetic particle morphology, size distribution, shape anisotropy, and magnetic domain size. The magnitude of H_c decreases with increase in Zn content. This behavior is similar to that of porosity. Porosity affects magnetization process because pores work as a generator of demagnetizing field. As the porosity decreases high field is needed to push the domain wall and thus Hc decreases.

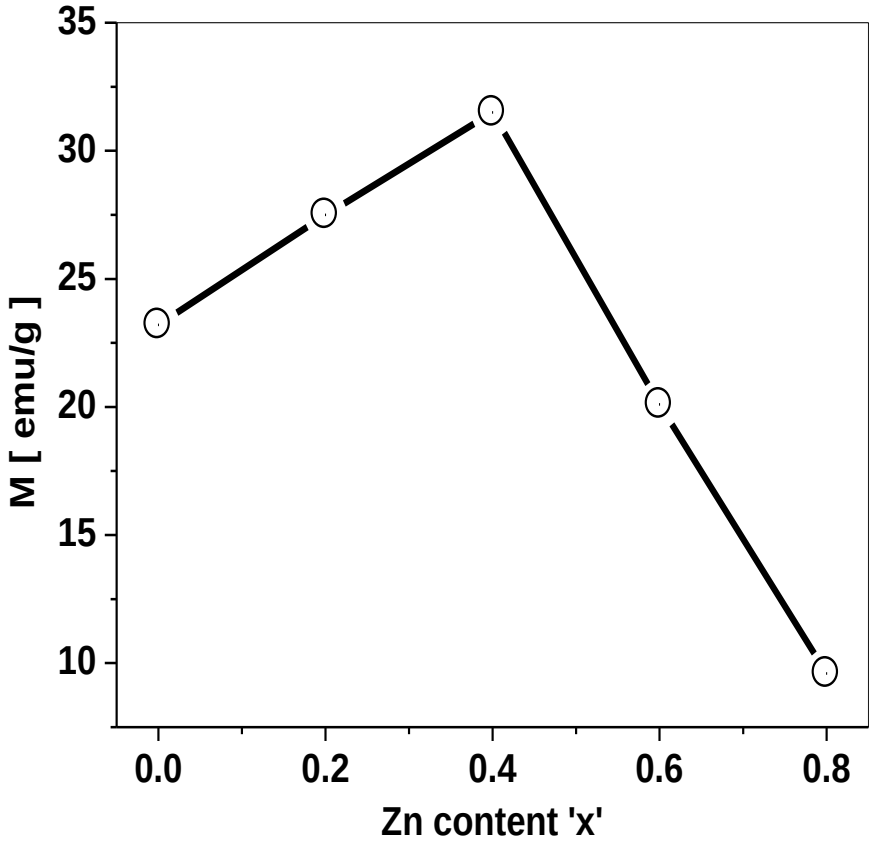

Fig. 5.11: Maximum magnetization values observed for $Cu_{1-x}Zn_xFe_2O_4$ (x = 0.0, 0.2, 0.4, 0.6, 0.8) nanoparticles from hysteresis loops.

It is known that the coercive force has a direct relation with the anisotropy constant of the sample, and, according to the one ion model, the anisotropy field of ferrites depends on the amount of Fe ions in the sample [23, 24]. In the present study, it seems that the amount of Cu^{2+} ions decreases as a result of increase in Zn^{2+} content. This means that the magneto anisotropy constant decreases with increase in Zn content and that, consequently, the magnitude of H_c also decreases. The observed magnetic properties of Cu-Zn nanoferrites were due to the combined effect of reduced particle size as well as with the increase of non-magnetic Zn content.

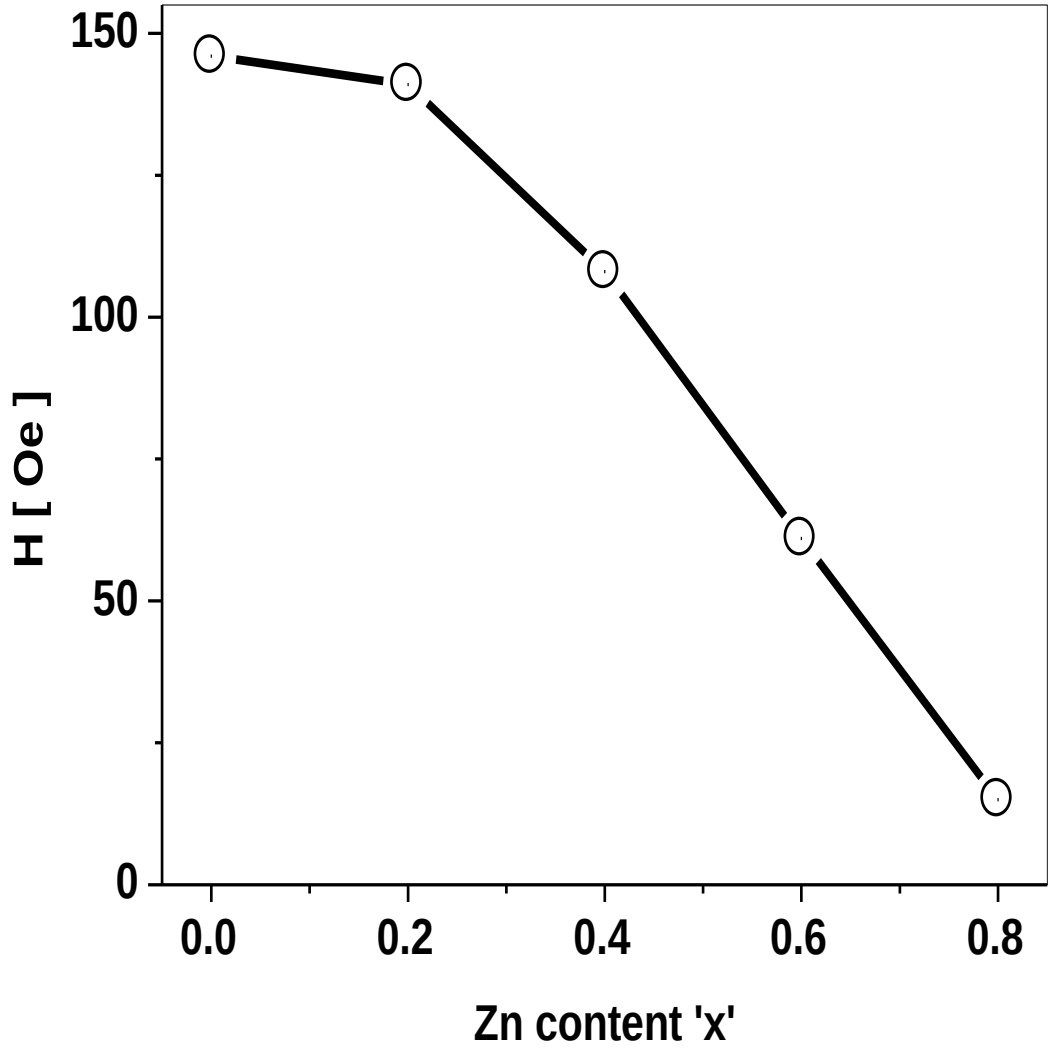

Figure 5.12: Coercivity (H_c) values observed for $Cu_{1-x}Zn_xFe_2O_4$ (x = 0.0, 0.2, 0.4, 0.6, 0.8) nanoparticles from hysteresis loops.

5.4 Conclusions

1. A series of $Cu_{1-x}Zn_xFe_2O_4$ (x = 0.0, 0.2, 0.4, 0.6, 0.8) nanoparticles were prepared using oxalic acid based precursor method.

2. The XRD analysis reveals the formation of single phase spinel structure at very low annealing temperature without any secondary phases.

3. The particle size was observed to decrease with increasing Zn concentration probably due to the reaction temperature and time.

4. The lattice parameters were observed to increase with increasing Zn content x, which is due to large ionic radii of zinc when compared to copper ions.

5. The two main spectroscopic bands corresponding to lattice vibrations were observed between 200 to 1000 cm^{-1}. These bands in IR were assigned to tetrahedral (A) and octahedral [B] groups. Respectively the spectroscopic bands shift towards the lower frequencies with the increasing Zn content x, which reveals that substitution of zinc is taking place in the spinels.

6. Magnetic measurements at room temperature for these samples revealed that magnetization at $\approx 1T$ do not change monotonically with the change of Zn content x.

7. The coercivity and remanence decreases with increasing non-magnetic Zn content x.

5.5 References

[1] Y. Suzuki, Annu. Rev. Mater. Res. 31 (2001) 265.

[2] M. Sugimoto, J. Am. Ceram. Soc. 82 (1999) 269.

[3] T. Tanaka, IEEE Trans. Magn. 35 (1999) 3010.

[4] J. Smit and H. P. J. Wijn, *Ferrites* _Philips Technical Library, Eindhoven, 1959.

[5] S. K. Pradhan, S. Bid, M. Gateshki and V. Petkov, Mater. Chem. Phys. 93 (2008) 224.

[6] A. R. Lamani, H. S. Jayanna, P. Parameshwara and R. Somasekhar, Ind. J. Pure and App. Phys. 47 (2009) 715.

[7] T. Tsoncheva, E. Manova, N. Velinov, D. Paneva, M. Popova, B. Kunev, et al., Cata. Commun. 12 (2010) 105.

[8] S.W. Tao, F. Gao, X.Q. Liu, O.T. Sørensen, Mater. Sci. Eng., B 77 (2000) 172.

[9] K. Faungnawakij, Y. Tanaka, N. Shimoda, T. Fukunaga, R. Kikuchi, K. Eguchi, Appl. Catal. B 74 (2007) 144.

[10] X. Zuo, A. Yang, C. Vittoria, V.G. Harris, J. Appl. Phys. 99 (2006) 08M909.

[11] C.W. Yao, Q.S. Zeng, G.F. Goya, T. Torres, J.F. Liu, J.Z. Jiang, J. Phy. Chem. C 111 (2007) 12274.

[12] D.G. Wickham, Inorg. Synth. 9 (1967) 152.

[13] A. T. Raghavender, S. E. Shirsath, K. Vijaya Kumar, J. Alloys. Comp. 509 (2011) 7004.

[14] A.T. Raghavender, D. Pajic, K. Zadro, T. Milekovic, P. Venkateshwar Rao, K.M. Jadhav, D. Ravinder, J. Magn. Magn. Mater. 316 (2007) 1.

[15] E. Auzans, D. Zins, E. Blums, R. Massart, J. Mater. Sci. 34 (1999) 1253.

[16] Patange SM, Shirsath Sagar E, Toksha BG, Jadhav SS, Shukla SJ, Jadhav KM. Appl Phys A 95 (2009) 429–434

[17] R.D. Waldron, Phys. Rev. B 99 (6) (1955) 1727.

[18] B.V. Bhise, M.B. Dongare, S.A. Patil, S.R. Sawant, J. Mater. Sci. Lett. 10 (1991) 922.

[19] Y.Yafet and C.Kittel , Phys. Rev ., 87 (1952) 290.

[20] S.V. Kakatkar, S.S. Kakatkar, R.S. Patil, A.M. Sankpal, S.S. Suryawanshi, D.N. Bhosale, S.R. Sawant, Phys. Status Solidi B. 198 (1996) 853.

[21] A.A. Sattar, H.M. El-Sayed, K.M. El-Shokrofy, M.M. El-Tabey, J. Mater. Eng. Perf. 14 (2005) 99.

[22] B. Parvatheeswara Rao, O. Caltun, W.S. Cho, Chong-Oh Kim, CheolGi Kim, J. Magn. Magn. Mater. 310 (2007) e812.

[23] S. Chikazumi, S. Charap, in: Physics of Magnetism, John Wiley and Sons, New York, 1964, pp.140.

[24] J.M.D. Coey, in: Rare Earth Permanent Magnetism,1st ed., John Wiley and Sons,New York, 1996, pp.220.